The Astrophysical Journal, 847:97 (11pp), 2017 October 1 https://doi.org/10.3847/1538-4357/aa886f

Robo-AO *Kepler* Asteroseismic Survey. I. Adaptive Optics Imaging of 99 Asteroseismic *Kepler* Dwarfs and Subgiants

Jessica S. Schonhut-Stasik[1,2], Christoph Baranec[1], Daniel Huber[1,3,4,5], Carl Ziegler[6], Dani Atkinson[1], Eric Gaidos[7], Nicholas M. Law[6], Reed Riddle[8], Janis Hagelberg[1], Nienke van der Marel[1], and Klaus W. Hodapp[1]
[1] Institute for Astronomy, University of Hawai'i at Mānoa, Hilo, HI 96720-2700, USA; jstasik@hawaii.edu
[2] University of Hertfordshire, Hatfield, Hertfordshire AL10 9AB, UK
[3] Sydney Institute for Astronomy (SIfA), School of Physics, University of Sydney, NSW 2006, Australia
[4] Stellar Astrophysics Centre, Department of Physics and Astronomy, Aarhus University, Ny Munkegade 120, DK-8000 Aarhus C, Denmark
[5] SETI Institute, 189 Bernardo Avenue, Mountain View, CA 94043, USA
[6] Department of Physics and Astronomy, University of North Carolina at Chapel Hill, Chapel Hill, NC 27599-3255, USA
[7] Department of Geology & Geophysics, University of Hawai'i at Mānoa, Honolulu, HI 96822, USA
[8] Division of Physics, Mathematics, and Astronomy, California Institute of Technology, Pasadena, CA 91125, USA
Received 2017 January 17; revised 2017 August 4; accepted 2017 August 22; published 2017 September 27

Abstract

We used the Robo-AO laser adaptive optics (AOs) system to image 99 main sequence and subgiant stars that have *Kepler*-detected asteroseismic signals. Robo-AO allows us to resolve blended secondary sources at separations as close as $\sim 0\farcs15$ that may contribute to the measured *Kepler* light curves and affect asteroseismic analysis and interpretation. We report eight new secondary sources within $4\farcs0$ of these *Kepler* asteroseismic stars. We used Subaru and Keck AOs to measure differential infrared photometry for these candidate companion systems. Two of the secondary sources are likely foreground objects, while the remaining six are background sources; however, we cannot exclude the possibility that three of the objects may be physically associated. We measured a range of i'-band amplitude dilutions for the candidate companion systems from 0.43% to 15.4%. We find that the measured amplitude dilutions are insufficient to explain the previously identified excess scatter in the relationship between asteroseismic oscillation amplitude and the frequency of maximum power.

Key words: asteroseismology – binaries: close – instrumentation: adaptive optics – methods: observational – stars: fundamental parameters – techniques: high-angular resolution

1. Introduction

Asteroseismology is the study of the internal structure of stars through the interpretation of their brightness oscillations (Aerts et al. 2010). As early as the seventeenth century, these variations in starlight were identified in stars with large amplitude brightness variations, such as Cepheids and other long-period variable stars (Holwards 1642). Asteroseismic behavior was initially studied only in the fundamental radial mode in which the star maintains spherical symmetry as it expands and contracts. It is now known that many stars pulsate both in radial and non-radial modes, including our own Sun. As well as advancing the understanding of variability, asteroseismology allows the determination of the fundamental properties of these stars, including density, radius, mass, and age (Chaplin et al. 2014; Metcalfe et al. 2014), and it has also led to discoveries relating to core properties and rotation rates (Bedding et al. 2011; Deheuvels et al. 2012).

It has been claimed that all stars with significant surface convection zones will feature oscillations (Handler 2013). Each observed frequency of oscillation probes an independent measure of an element of the stellar structure, so the more modes for which oscillations are detected, the more information we gather about the star (Christensen-Dalsgaard 2014). Consecutive oscillation modes are often too close in frequency to be distinguished using ground-based observations. Therefore, observations need to take place above the atmosphere to resolve these consecutive modes. Many past and present space-based missions have contributed to the field of asteroseismology including the *Wide-field InfraRed Explorer (WIRE)* (Hacking et al. 1997), the *Microvariability and Oscillations of Stars Telescope (MOST)* (Walker et al. 2003), the *COnvection, ROtation and planet Transits* mission *(CoRoT)* (Auvergne et al. 2009), the *BRIght Target Explorer (BRITE)* (Schwarzenberg-Czerny et al. 2010) and the *Kepler* mission (Borucki et al. 2010). *Kepler* alone has revolutionized asteroseismology as a result of its extensive target sample, near continuous monitoring capability, and increased photon collection power.

Approximately 17,000 stars that demonstrate solar-like oscillations have been observed in short- and long-cadence by the *Kepler* mission (Bedding et al. 2010; Hekker et al. 2011; Huber et al. 2011; Mosser et al. 2012; Stello et al. 2013). These data are exploited in a number of ways, including the examination of oscillation frequencies in *Kepler* planet host stars (Davies et al. 2016) and studying oscillation mode linewidths and mode heights (Appourchaux et al. 2014). The quality of the reduced *Kepler* asteroseismic data is also improving, e.g., by mitigating the impact of the regular gaps in the data (García et al. 2014).

Despite the advantages of *Kepler*, unresolved secondary sources within the *Kepler* photometric apertures can affect our ability to measure asteroseismically determined stellar properties. This occurs when the radiant flux from the secondary star dilutes the frequency amplitudes in the primary light curve. For example, Campante et al. (2014) sets lower limits for the surface gravity of planet candidate host stars, provided no solar-like oscillations are detected. If an unidentified secondary source was masking solar oscillations this would result in an inaccurate lower limit for surface gravity.

For an asteroseismic star with a physically bound companion, more aspects of the systems can be studied, e.g., Lai (1997),

Springer & Shaviv (2013), and Polfliet & Smeyers (1990) find that tides in close systems can cause the stars to induce or disturb pulsations in one another. Physically associated equal-mass binary stars are likely to follow the same evolutionary path and will display similar oscillation frequencies that may overlap. From the oscillations alone, one may not be able to determine if the target is a binary star or a single hybrid pulsator.

Adaptive optics (AO) can be used to identify the binary companions and background objects to asteroseismic stars at separations unavailable to spectroscopic or seeing-limited observations. Campante et al. (2015) used Robo-AO to measure the amount of dilution of the asteroseismic target Kepler-444 in the visible *Kepler* bandpass by an M dwarf spectroscopic binary system 1.″9 away. Further observations by Dupuy et al. (2016) with Keck AO were unable to resolve the individual components of the M dwarf pair and confirmed the absence of additional fainter nearby sources.

While a handful of asteroseismic stars have been imaged with AO, here we report the first systematic AO survey of asteroseismic stars. We used Robo-AO to observe 99 *Kepler* stars displaying oscillations to determine the existence of any blended binary companions[9], which may be contributing to the stellar light curve. We then used Keck and Subaru AO to obtain differential infrared (IR) photometry in order to determine the spectral types of each candidate companion. A subset of these systems was also observed spectroscopically for more accurate constraints on their spectral types.

The work is organized as follows. Section 2 describes the target selection and observations. The data reduction and analysis is discussed in Section 3. The analysis of stellar properties is described in 4. In Section 5, we review the results of the survey, the discoveries have made, follow-up measurements, and target confirmation. Section 6 discusses the impact of these results and further analysis. Conclusions and future work are noted in Section 7.

2. Target Selection and Observation

2.1. Target Selection

To determine if *Kepler* targets demonstrated detectable oscillations, short-cadence data of ∼2000 solar-like stars were provided to the asteroseismic community (Chaplin et al. 2010; Gilliland et al. 2010; Huber et al. 2011; Verner et al. 2011). Approximately 500 solar-like stars were found to display observable oscillations (Chaplin et al. 2010; Verner et al. 2011), and the *Kepler* Community Follow-up Observation Program (CFOP) compiled these stars into a list of "standard stars." Each star in the list was assigned a priority of either Platinum or Gold. Platinum stars have full-mission, short-cadence data. Gold stars have lower signal-to-noise (S/N) asteroseismic detections, e.g., a month of short-cadence data. We selected the Platinum sample for our initial AO survey with the intention of observing the full Gold priority sample in later work. Ultimately, our target sample contains 97 Platinum and two Gold stars due to a reevaluation of the S/N quality of two targets by CFOP. Seven of the observed platinum standard stars are also *Kepler* Objects of Interest (KOIs), which are stars that show repeating transit signals. The target sample is detailed in Table 4.

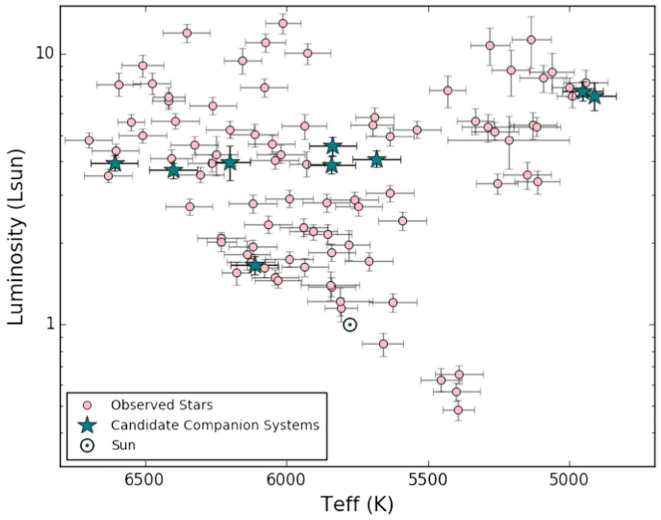

Figure 1. H-R diagram of our target sample with green stars showing the nine candidate companion systems detected. Our sample of stars span a broad area of the lower main sequence/red giant branch. At least two of the candidate companion systems have subgiant primaries which display a high temperature and luminosity. The Sun is shown for reference.

The stars in our sample are solar-like with effective temperatures between 4910 and 6700 K. Solar-like stars are most likely to display stochastic oscillations as opposed to the coherent pulsations seen in hotter stars. These solar-like oscillations are predominantly acoustic waves (p-modes) that propagate via the compression and rarefaction of gas, with the pressure gradient acting as the restoring force. Because oscillations in solar-like main sequence stars usually have periods of ∼5–13 minutes, multiple periods can be resolved by *Kepler* in short-cadence mode.

Stars with greater apparent brightness are more easily observed due to increased signal, and stars with higher luminosity are more likely to demonstrate observable oscillations because oscillation amplitudes increase proportionally with luminosity (Kjeldsen et al. 1995; Huber et al. 2011). The standard stars list contains bright stars relative to the entire *Kepler* Input Catalog (KIC). The stars in our target sample have i' magnitudes from 7.1 to 11.3.

Figure 1 shows the sample on a Hertzsprung–Russell (H-R) diagram. We used the CFOP catalog[10] to obtain the targets' effective temperatures and radii, with errors, and with the exception of KIC 8760414. The luminosity errors were determined using the errors in temperature and radius. The majority of target stars fall on the early-to-mid main sequence, or low on the red giant branch.

2.2. Observations

2.2.1. Robo-AO

We used the Robo-AO robotic visible-light laser AO system (Baranec et al. 2013, 2014), mounted on the 1.5 m telescope (Cenko et al. 2006) at Palomar Observatory, to obtain high-angular-resolution images of the 99 asteroseismic stars comprising the target sample. We used a queue scheduled mode (Riddle et al. 2014) to perform all observations

[9] In this paper, a candidate companion system is used to describe any visible multiple star system, including where the secondary star is an unassociated asterism and a binary system are two physically associated stars. Binary fraction is used to define the number of physically associated stars, whereas candidate companion fraction includes all visual candidate companion systems.

[10] https://exofop.ipac.caltech.edu/cfop.php

Table 1
Robo-AO Specifications

Sample targets	99
Exposure time	90 s
Observation wavelength	i' band
FWHM resolution	$0\farcs15$
Field of view	$44'' \times 44''$
Pixel scale	43.1 mas pix^{-1}
Detector format	1024^2 pixels
Number of nights	18
Observation date range	2014 July 15–November 7

contemporaneous with other science programs. Observations took place between 2014 June 15 and 2014 November 7, across 18 nights, with some objects observed more than once to ensure high-quality images. For targets observed multiple times, we indicate the date of the highest-quality observation. Table 1 identifies the survey and system specifications.

The raw images comprise a sequence of full-frame-transfer detector reads from an electron multiplying CCD at a rate of 8.6 Hz. We used a total exposure time of 90s that enables the detection of additional sources of up to ∼6 magnitudes fainter than the target (Law et al. 2014). We took all observations in the i' filter to obtain the sharpest possible images, allowing Robo-AO to detect secondary sources within $0\farcs15$ for bright targets ($m < 13$) in median seeing conditions.

2.2.2. Keck Adaptive Optics

We used the NIRC2 IR camera behind the Keck II AO system to confirm potential secondary sources and obtain supplementary differential near-IR photometry. These observations took place on 2016 April 23, and September 12 and 13. We operated NIRC2 in its 9.9 mas pixel^{-1} mode which results in a field of view of $\sim 10\farcs0$. We used the the Brγ filter (central wavelength 2.17 μm) for all observations. We obtained three-point dithered images for each star with total exposure times from 45 to 180 s.

2.2.3. Subaru Adaptive Optics

We used the Infrared Camera and Spectrograph (IRCS) behind the Subaru AO system to observe the candidate companions not observed with NIRC2. These observations took place on 2016 June 17. We used IRCS in the 20.57 mas/pixel mode which results in a field of view of $21\farcs06$. We took many of these images in poor conditions due to variable weather on the night. We used a K' filter (central wavelength 2.12 μm) and obtained multi-point dithered images with total exposure times from 1 to 84 s.

2.2.4. Visible-light Spectroscopy

Integral field, visible-wavelength spectra of 8 candidate systems were obtained with the Super Nova Integral Field Spectrograph (SNIFS) on the UH 2.2 m telescope on Maunakea on 2016 April 28 and 2016 May 2. Seeing was typically $0\farcs7$–$1\farcs1$. SNIFS has a $6'' \times 6''$ field of view (15×15 pixels) with a 320–970 nm spectral range in two channels (B and R) at a resolution of 700–1000 (Aldering et al. 2002; Lantz et al. 2004). We used integration times of 1–2 minutes. Flat-field images and Th-Ar spectra were obtained at each pointing to permit accurate calibration of the spectra.

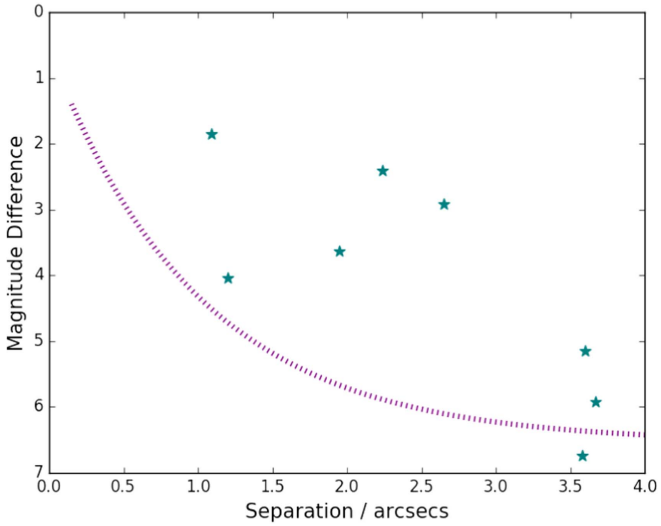

Figure 2. Points on this plot show the angular separations and magnitude differences of the detected secondary sources described in Tables 2 and 3. The dotted line represents the typical 5σ i'-band contrast curve achieved during the observations with Robo-AO.

3. Data Reduction

We used the standard Robo-AO data reduction techniques described in Law et al. (2014). We calibrated and registered individual frames to synthesize a deep exposure image, before running a fully automated point-spread function (PSF) subtraction and companion detection routine. We used the additional IR images and photometry to fit a spectral type to each star and calculated the estimated photometric distances for the candidate companion star. We used spectroscopy to determine the spectral types for some stars.

3.1. Data Reduction and Imaging Pipeline

The Robo-AO data reduction pipeline subtracts a dark frame and calibrates the flat field from each raw frame. We align calibrated frames on the position of the target star then stack them together to create a single reduced image. We manually inspected the reduced images and flagged possible companions within the size of a *Kepler* pixel, $\sim 4''$. We do not report secondary sources at greater separations, as seeing-limited observations can detect these.

3.2. Imaging Performance Metrics

Previous analysis of reduced Robo-AO images has shown that the measured width of the core point source function (PSF) is an excellent indicator of achievable contrast performance (Law et al. 2014). We fit two Moffat functions to the PSF of each observation, one tuned to the PSF core and the other to the uncorrected halo. If the FWHM of the core was $\geqslant 0\farcs14$, the image quality and achievable contrast was in the top 30th percentile of all useful Robo-AO observations. If the data obtained for any particular observation did not meet these criteria, the observation was repeated until it did. This ensured homogeneous achievable contrast across the entire survey. The typical 5σ achievable contrast for Robo-AO images for this survey is shown in Figure 2.

Table 2
Detected Companion Systems

KIC ID	Separation (″)	Position Angle (°)	Magnitude Difference i'	Magnitude Difference K'	i' Detection Significance (σ)	Spectral Type[b]	Amplitude Dilution i' (%)	Amplitude Dilution K' (%)	IR Data
5955122	3.60 ± 0.06	257.7 ± 1.6	5.15 ± 0.01	4.30 ± 0.02	4.46	F9IV-V	0.86 ± 0.01	1.87 ± 0.05	Subaru
7584900	2.24 ± 0.06	39.2 ± 1.7	2.40 ± 0.01	2.61 ± 0.04[a]	21.9	K3IV[c]	9.90 ± 0.11	8.26 ± 0.37	Keck
7747078	2.65 ± 0.06	259.8 ± 1.6	2.92 ± 0.01[d]	2.86 ± 0.02	27.1	F9IV-V	6.35 ± 0.10	6.71 ± 0.15	Subaru
8394589	1.95 ± 0.06	198.0 ± 1.8	3.63 ± 0.01	2.36 ± 0.02	8.86	F8V	3.41 ± 0.05	10.2 ± 0.29	Subaru
9139163	3.58 ± 0.06	291.7 ± 1.6	6.74 ± 0.01	4.77 ± 0.02	6.99	F8IV	0.20 ± 0.004	1.23 ± 0.03	Subaru
9206432	3.67 ± 0.06	21.4 ± 1.6	5.92 ± 0.01	5.61 ± 0.01[a]	4.81	F8IV	0.43 ± 0.003	0.57 ± 0.01	Keck
11026764	1.09 ± 0.06	81.0 ± 2.2	1.85 ± 0.01	2.22 ± 0.02	5.05	G1V	15.4 ± 0.22	11.5 ± 0.24	Subaru
11554100	1.20 ± 0.06	259.3 ± 2.1	4.04 ± 0.05	4.05 ± 0.02[a]	<3	K3IV[a]	2.46 ± 0.15	2.34 ± 0.07	Keck

Notes.
[a] Filter: Brγ.
[b] Values taken from KASOC: http://kasoc.phys.au.dk.
[c] Values not found on KASOC. Individual magnitude values for J, H, K', and i' taken from CFOP (https://exofop.ipac.caltech.edu/cfop.php) and used in conjunction with the code from Atkinson et al. (2017) to determine a composite type.
[d] Composite value of system not available on CFOP. J, H and K', values from CFOP used with Atkinson et al. (2017) models to determine i'.

3.3. PSF Subtraction

We used a custom locally optimized PSF subtraction routine based on the Locally Optimized Combination of Images algorithm (Lafrenière et al. 2007) to identify close secondary sources. A reference PSF was created by using a set of twenty observations taken from observations of other stars, imaged in the same filter and closest in observation time to the target observation. The reference PSF was subtracted from the original image, leaving residuals consistent with photon noise.

3.4. Automated Companion Detection and System Confirmation

We used an automated companion detection algorithm developed for our Robo-AO KOI surveys (see Ziegler et al. 2016) to detect additional companions not identified in the raw or PSF-subtracted data. The significance was found for each candidate companion by sampling and modeling the background noise level as a function of radial distance from the target star. We then slid an aperture of the diffraction-limited FWHM diameter along concentric annuli centered on the target star. Possible astrophysical detections are identified when the enclosed flux of the aperture becomes significantly greater than the local noise. In this sample of brighter stars, bright speckles produce the majority of high-significance detections, which we manually discard.

3.5. Reduction of IR AO Images

Each dithered image from NIRC2 and IRCS was subject to sky subtraction and flat-field calibration. Each frame was corrected for bad pixels and stacked to create final images.

3.6. Spectroscopy Reduction

Extraction and processing of spectra are described in Aldering et al. (2002) and Mann et al. (2015). Spectra of identified sources were extracted manually and the distance in pixels computed. The position of the primary source in each image "slice" (specific wavelength) plus the offset was used to place an aperture on each slice allowing us to obtain photometry of the fainter secondary. Aperture photometry was performed on each image slice after subtracting Gaussian fits to the primary. Corrections to the photometry used the atmospheric extinction of Buton et al. (2013) and additional corrections described in Mann et al. (2015). Spectra were dereddened and compared (minimizing χ^2) with the Göttingen spectral library, which was generated by the PHOENIX model in spherical mode (Husser et al. 2013). Because of low signal in the B channel and lack of photometry to accurately match the two channels, only the R channel was used. Several narrow wavelength ranges that are difficult to model or have strong telluric absorption lines were also excluded (see Mann et al. 2013). We adopted the estimated extinction values for each of the targets from the KIC catalog, with the caveat that the actual values could be much larger if the sources are not physical companions.

4. Analysis of Stellar Properties

We measured the relative astrometry and photometry and determined the spectral types for each of the discovered candidate companion systems. We then used this information to determine the distance to each candidate companion star and calculated the possibility of physical association of these systems. We also report the oscillation amplitude dilution due to the radiant flux of the secondary star. These results are summarized in Tables 2 and 3.

4.1. Relative Astrometry

We determined the separation and position angle between the primary and secondary stars, which includes a correction for optical distortion by using the solution produced from Robo-AO measurements of globular clusters detailed in Riddle et al. (2015). The PSF-subtracted images were used to find the position of the secondary relative to the primary for the companions found at a detection significance of $<3\sigma$.

4.2. Photometry and Individual Spectral Types

We used aperture photometry to determine magnitude differences for all the candidate companion systems in both i' and K'. The images are high resolution and with well-separated companions, so the brightness of each star can be measured using simple aperture photometry. We corrected for the radiant flux of the primary PSF halo by subtracting an aperture on the opposite side of the candidate companion star. Errors for the companion photometry were estimated using a varying aperture

Table 3
Individual Star Information for Companion Systems

KIC ID	Primary Magnitude i' and K'	Secondary Magnitude i' and K'	Spectral Type Primary	Spectral Type Secondary	Radius Secondary ($R_\odot$)	Distance Primary[c] (pc)	Error[d]	Distance Secondary (pc)	Error	Overlap Within Error
5955122	9.13 ± 0.03	14.3 ± 0.03	F7V	M4V[a]	0.88 ± 0.01	169.0	+8.4	80[a]	+20	NO
	7.94 ± 0.05	12.2 ± 0.05					−7.6		−20	4.13σ
7584900	11.1 ± 0.02	13.5 ± 0.02	K3IV	K2V[b]	0.93 ± 0.02	499.3	+32.5	339	+32	…
	9.19 ± 0.08	11.8 ± 0.08					−51.1		−24	2.24σ
7747078	9.25 ± 0.03	12.2 ± 0.03	F7V	G3	1.11 ± 0.08	170.3	+7.4	340	+53	NO
	8.05 ± 0.04	10.9 ± 0.04					−8.2		−43	4.01σ
8394589	9.43 ± 0.03	13.1 ± 0.03	F5V	K8V[b]	0.79 ± 0.01	116.9	+5.2	147	+7	NO
	8.34 ± 0.05	10.7 ± 0.05					−5.2		−7	3.69σ
9139163	8.21 ± 0.04	15.0 ± 0.04	F3IV-V	M3	0.42 ± 0.04	97.4	+8.5	150	+20	…
	7.24 ± 0.04	12.0 ± 0.04					−8.5		−19	2.53σ
9206432	8.98 ± 0.01	14.9 ± 0.01	F2IV-V	F9	1.17 ± 0.04	137.2	+4.1	1300	+120	NO
	8.07 ± 0.03	13.7 ± 0.03					−5.5		−170	6.84σ
11026764	9.29 ± 0.03	11.2 ± 0.03	G4V	F3V	1.33 ± 0.03	172.1	+16.2	393	+31	NO
	8.00 ± 0.04	10.2 ± 0.04					−16.2		−29	7.07σ
11554100	11.1 ± 0.11	15.1 ± 0.11	K3IV	K3	0.91 ± 0.02	442.5	+75.8	632	+50	…
	9.25 ± 0.05	13.3 ± 0.05					−21.9		−33	2.36σ

Notes.
[a] Value from the spectroscopic data.
[b] Spectroscopic values corroborate with the photometric values here.
[c] Corrected for the effects of amplitude dilution.
[d] Errors include propagation of amplitude dilution errors.

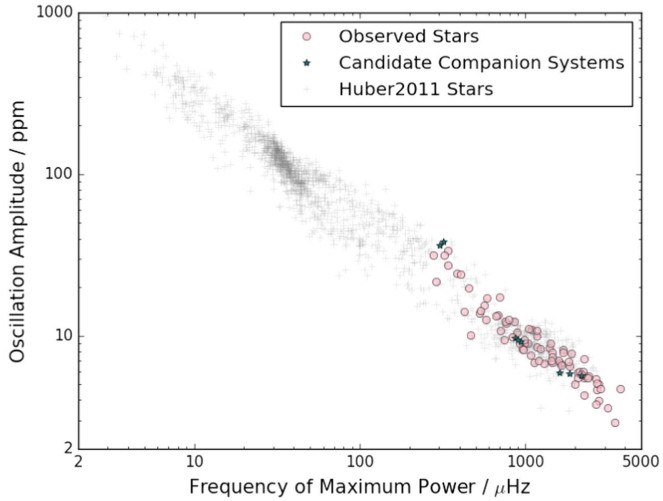

Figure 3. Oscillation amplitude vs. frequency of maximum power for all stars in Huber et al. (2011; gray), all targets observed in our AO survey (pink circles), and all targets in the survey with detected secondary sources (green stars). Error bars are omitted for clarity, but are found in Huber et al. (2011).

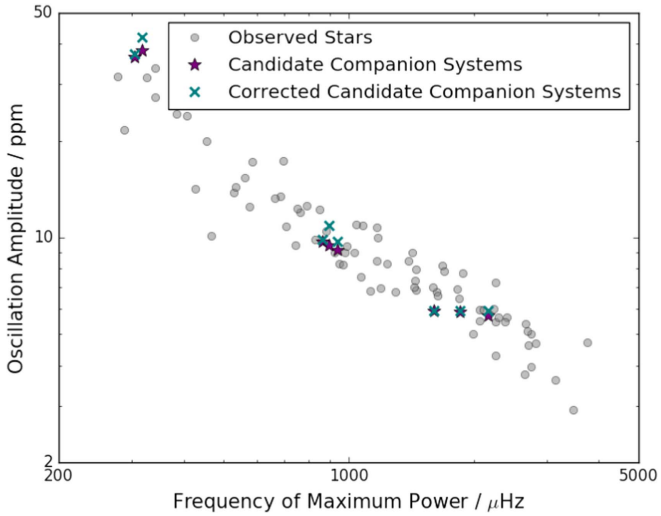

Figure 4. Oscillation amplitude vs. maximum oscillation frequency for targets in our sample. Candidate companion systems are shown before (purple stars) and after (green crosses) correction for the amplitude dilution from secondary sources.

with the width of the stellar PSF and measuring the standard deviation of the difference.

We compared the spectral types determined through our photometry with the blended system spectral types available on *Kepler* Asteroseismic Science Operations Center (KASOC) online database.[11] We found the spectral types of six of the candidate companion systems on KASOC: five F stars and one G star. The spectral types for the remaining two candidate companion systems were not available, so we used apparent magnitudes for the J, H, K', and i' bands from the CFOP catalog and fit them to a catalog of main sequence standards from Kraus & Hillenbrand (2007) using code developed by Atkinson et al. (2017). This resulted in two K candidates, KIC 7584900 and KIC 11554100, with effective temperatures of 4960 K and 5150 K, respectively. The primary star dominates the radiant flux in each system and we found that our fit primary spectral types are consistent with the candidate companion system spectral types from KASOC/CFOP. The luminosity classes assigned to these two K subgiants are from asteroseismology.

We used the KIC magnitudes listed on CFOP as the combined apparent magnitude of the blended primary and secondary star. We determined the individual stellar magnitudes for the primary and secondary stars from the combined apparent magnitude and our measured magnitude differences.

[11] http://kasoc.phys.au.dk

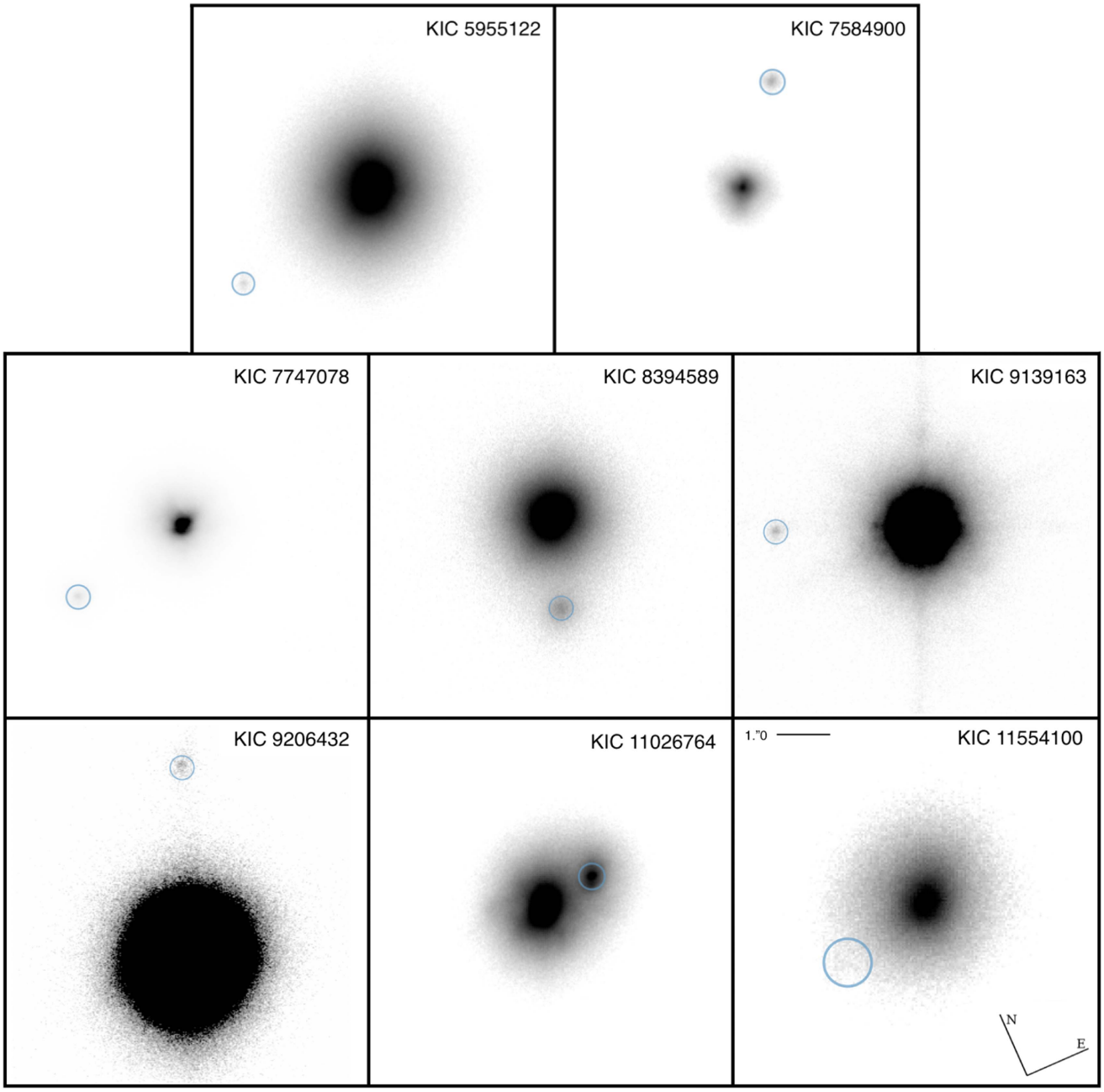

Figure 5. Robo-AO i'-band images of discovered candidate companion systems. The secondary source is outlined in blue circle. Scale and orientation shown at bottom right.

We then used the individual magnitude values to fit the spectral type of each each star. Measured photometry and uncertainties generate Gaussian distributions of *i–K* and *Kepler–K*. Photometric values are weighted by measured uncertainty and are then corrected for reddening using existing *A_V* values and standard absorption relations (Cardelli et al. 1989). The Atkinson et al. (2017) model only fits to main sequence stars and does not take into account age or metallicity, nor does it discriminate between dwarf and giant stars. We infer the radius from the spectral fit to the secondary source assuming they are all dwarfs.

4.3. Amplitude Dilution

Radiant flux from a companion star in an unresolved binary system will contaminate the *Kepler* light curve, reducing the relative amplitude signal, hindering the determination of oscillation frequencies. Using the relative photometry between the primary and the secondary stars we determined the amplitude dilution, A,

$$A = \frac{f_2}{f_1 + f_2}, \quad (1)$$

in the i' and K' bands, where f_1 and f_2 denote the radiant flux of the primary and secondary star, respectively.

4.4. Estimation of Photometric Distances

We used the target distances determined by Mathur et al. (2017), who revised stellar properties for almost 200,000 *Kepler* stars using isochrone fitting. To determine the corrected

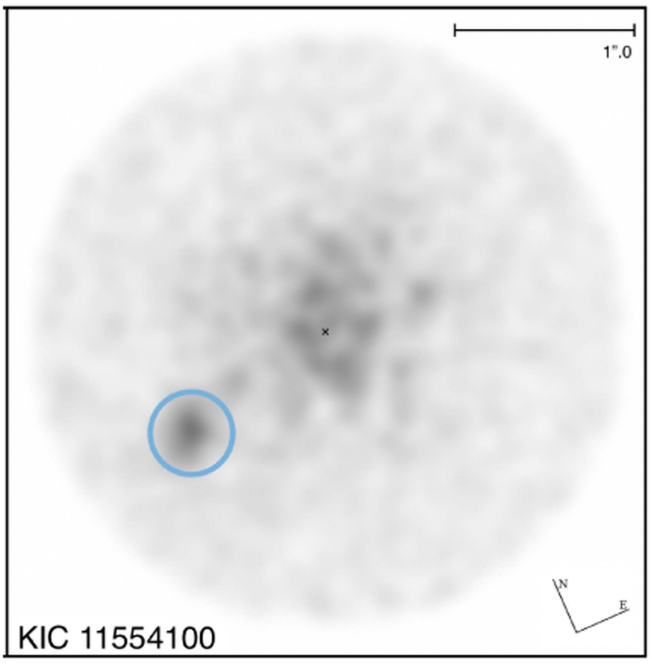

Figure 6. PSF-subtracted Robo-AO image of KIC 11554100. The image has been convolved with a diffraction-limited Gaussian kernel for clarity. The location of the primary star is indicated with an ×.

distance to the primary, we subtract off the measured radiant flux of the secondary in i' and recalculate the distance,

$$d_{\text{corrected}} = \sqrt{\frac{1}{1-A}}\, d_{\text{blended}}, \quad (2)$$

where $d_{\text{corrected}}$ is the corrected distance to the primary star and d_{blended} is the distance reported by Mathur et al. (2017) of the blended system. To calculate the distances to the secondary sources, we used the standard distance modulus equation with our measured apparent magnitudes and the absolute magnitudes derived from our fit of spectral type.

By comparing whether the distances to the primary and secondary stars overlap within measurement error, we are able to determine whether the stars can be physically associated. From the derived distance measurements, we calculated the significance of the difference in distances. For values $>3\sigma$, these systems are likely to be physically unassociated. For a confidence level less than this, we cannot rule out the possibility of physical association.

5. Discoveries

We initially found 11 candidate companion sources within 4.″0 of the 99 *Kepler* standard stars we observed with Robo-AO. Three of the target sample stars, all KOIs, have had secondary sources previously detected that were fainter than our survey sensitivity. These are noted in Table 4. We found seven in the initial manual search of reduced images and another four in the PSF-subtracted images. We then used NIRC2 and IRCS to observe all of these candidates (see Table 5), and ruled out three of the candidate secondary sources found from PSF-subtracted images. The Robo-AO discovery images are summarized in Figure 5 with the companion found in the PSF-subtracted image, KIC 11554100, shown in Figure 6. The IRCS and NIRC2 are shown in Figures 7 and 8, respectively.

5.1. Spectroscopy

We were only able to extract the spectra for three of the secondary sources due to decreased achievable contrast ratio with the seeing-limited SNIFS instrument. We find that the secondary to KIC 5955122 has a spectrum consistent with that of a late-type ($T_e \approx 3200$ K), metal-poor ([Fe/H] ≈ -0.5), M dwarf, with an indication of Hα in emission (See Figure 9). The secondary sources to KIC 7584900 and 7747078 have spectra that match hotter dwarfs, with $T_e \sim 5900$ and 6500 K, respectively, but with large uncertainties.[12] *B*-band fluxes from both of these stars are significantly attenuated with respect to the best-fit models, suggesting that extinction along the line of sight is much higher and, possibly, the stars are more distant and unrelated to the targets. Values derived from spectroscopy are noted in Table 3.

5.2. Are Secondary Stars Background/Foreground Objects?

We calculated the probability of the eight candidate companions not being associated using their photometric distances (see Table 3). We found six of these candidate companions are likely to be background sources, although we cannot rule out that KICs 9139163 and 11554100 may be potentially physically associated. The remaining two candidate companions are likely foreground objects, however KIC 7584900 may be physically associated. It is possible that these secondary sources could be very distant giants as opposed to nearby dwarfs.

6. Discussion

6.1. Impact on Stellar Oscillation Amplitudes

By studying stellar oscillation amplitudes, we gain insight into the poorly understood physics of surface convection that cause the stochastic excitation and damping of solar-like oscillations (e.g., Houdek et al. 1999). Over the last two decades, a consensus emerged that oscillation amplitudes scale as a function of luminosity, temperature, and mass with different power-law coefficients (Kjeldsen et al. 1995; Huber et al. 2011; Stello et al. 2011; Corsaro et al. 2013). Despite the recent advances due to the large sample observed by *Kepler*, the residual scatter of amplitude scaling relations remain significantly larger than the measurement uncertainties. Huber et al. (2011) shows a standard deviation of the oscillation amplitudes that is 2.4 times larger than the median uncertainty. This suggests that the errors do not explain the scatter, which implies an as of yet unidentified additional physical mechanism influencing oscillation amplitudes.

We binned the values of frequency of maximum power from Huber et al. (2011) to widths of 100 μHz and calculated the ratio of amplitude standard deviation to average measurement error for each bin. All but one bin produced a result greater than 1, with a range of 0.9–9.5, implying the scatter of the amplitude measurements exceeds measurement error. The binned values produce a ratio of standard deviation to measurement error of 3.0.

The presence of undetected companions or secondary sources to these asteroseismic stars could provide an explanation for the additional scatter seen in the predictions of

[12] SNIFS spectra readily resolve the broad molecular features of late K and M dwarfs, but not the atomic lines that are important temperature indicators in the spectra of hotter stars.

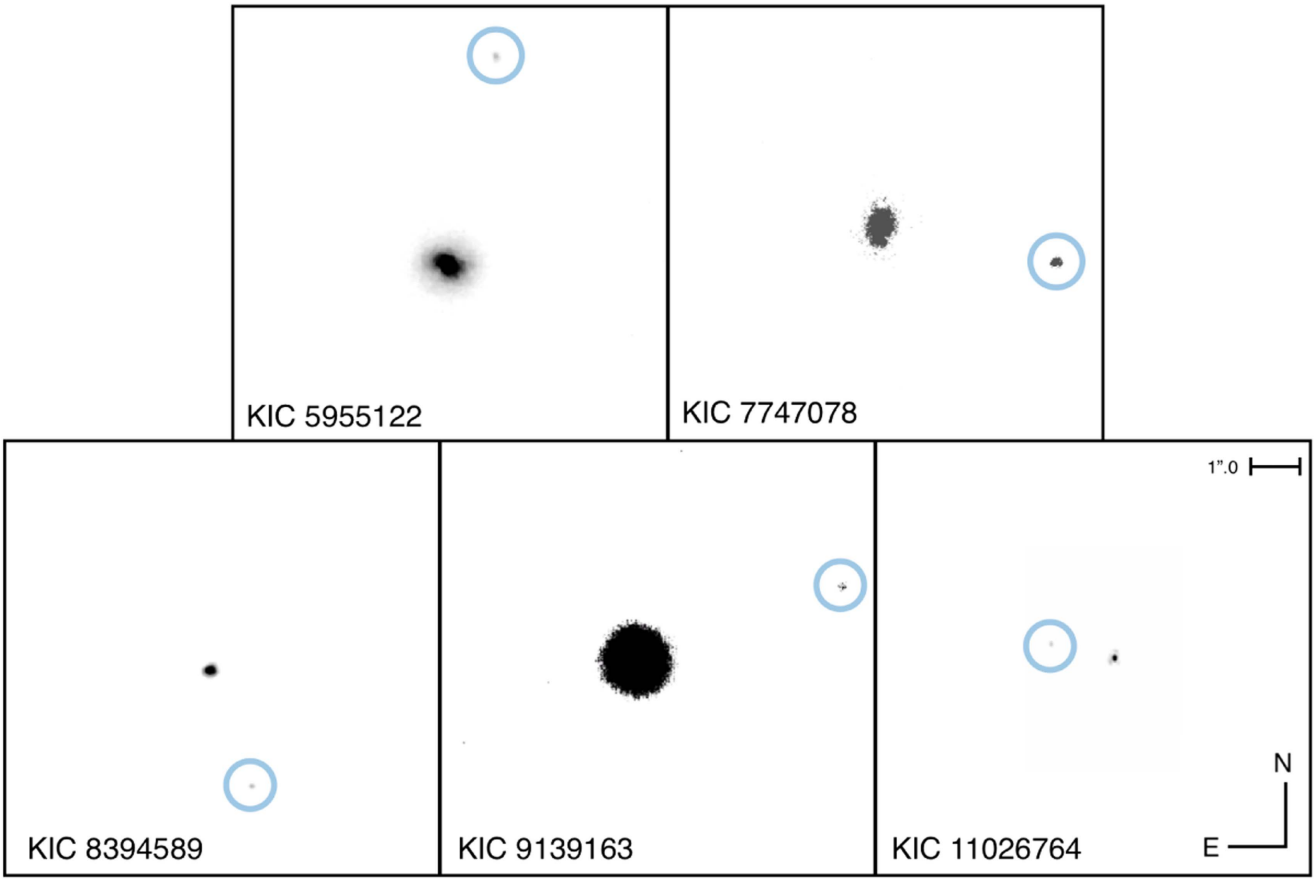

Figure 7. IRCS K'-band images of stars with detected secondary sources.

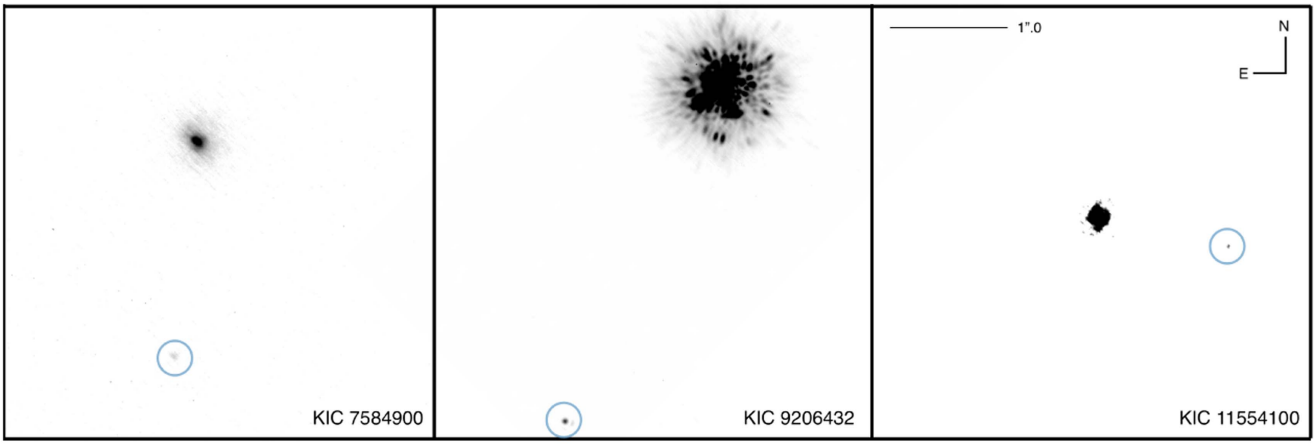

Figure 8. NIRC2 Brγ images of stars with detected secondary sources.

oscillation amplitude. These secondaries contribute additional radiant flux and hence cause a systematic dilution of the observed amplitudes in the *Kepler* bandpass. To test this, we have used the asteroseismic data from Huber et al. (2011), whose target sample contains all our candidate companion systems. Figure 3 shows the relation between oscillation amplitude and the frequency of maximum power ($\nu_{\rm max}$) for the full Huber et al. (2011) sample. For clarity, Figure 4 shows only stars included in our survey and the oscillation amplitudes after correcting for the amplitude dilution by secondary sources. The correction of amplitude dilution has a negligible effect on the overall scatter of oscillation amplitudes versus the frequency of maximum power. Fainter sources below our sensitivity limit will have amplitude dilutions of $<1\%$ which will have an even smaller impact on the scatter. Therefore, the presence of stellar companions to asteroseismic stars is unlikely to be the sole cause of the large scatter.

6.2. Comparison of the Detected Companion Fraction with the Robo-AO Kepler Planetary Candidate Survey

We compared the candidate companion fraction from this, the asteroseismic sample with the Robo-AO *Kepler* Planetary

Table 4
Full Robo-AO Observation List

KIC ID	$m_{i'}$ (mags)	Obs. Date	Companion?	KOI
1435467	8.7	2014 Jul 13	⋯	⋯
2837475	8.4	2014 Jul 13	⋯	⋯
2852862	10.6	2014 Jul 13	⋯	⋯
3424541	9.6	2014 Jul 11	⋯	⋯
3427720	9.0	2014 Jul 11	⋯	⋯
3632418	…	2014 Jul 13	A+	K00975.01
3656476	9.3	2014 Jul 13	⋯	⋯
3735871	9.6	2014 Jul 13	⋯	⋯
4351319	9.6	2014 Jul 13	⋯	⋯
4914923	…	2014 Jul 13	⋯	⋯
5184732	8.0	2014 Jul 13	⋯	⋯
5596656	9.2	2014 Jul 18	⋯	⋯
5607242	10.5	2014 Jul 13	⋯	⋯
5689820	11.0	2014 Jul 13	⋯	⋯
5723165	10.3	2014 Aug 28	⋯	⋯
5955122	9.1	2014 Jul 13	Yes	⋯
6064910	11.3	2014 Jul 12	⋯	⋯
6106415	…	2014 Sep 1	⋯	⋯
6116048	8.3	2014 Jul 13	⋯	⋯
6225718	…	2014 Aug 20	⋯	⋯
6442183	…	2014 Jul 13	⋯	⋯
6531928	10.4	2014 Jul 13	⋯	⋯
6603624	8.9	2014 Jul 13	⋯	⋯
6679371	8.7	2014 Jul 13	⋯	⋯
6693861	11.3	2014 Sep 2	⋯	⋯
6766513	11.2	2014 Jul 13	⋯	⋯
6933899	9.4	2014 Sep 1	⋯	⋯
7103006	8.8	2014 Jul 13	⋯	⋯
7107778	11.1	2014 Jul 13	⋯	⋯
7206837	9.7	2014 Jul 13	⋯	⋯
7296438	9.9	2014 Jul 12	CFOP	K00364.01
7341231	…	2014 Jul 18	⋯	⋯
7584900	11.0	2014 Jun 19	Yes	⋯
7680114	9.9	2014 Jul 13	⋯	⋯
7747078	…	2014 Jul 13	Yes	⋯
7771282	10.6	2014 Jul 13	⋯	⋯
7799349	9.2	2014 Sep 2	⋯	⋯
7800289	9.4	2014 Jun 19	⋯	⋯
7871531	9.0	2014 Jun 19	⋯	⋯
7970740	7.6	2014 Aug 28	⋯	⋯
7976303	8.9	2014 Jul 13	⋯	⋯
8006161	7.1	2014 Jun 17	⋯	⋯
8018599	…	2014 Jul 13	⋯	⋯
8179536	9.4	2014 Jul 13	⋯	…
8179973	10.0	2014 Jul 13	CFOP	K01019.01
8228742	9.2	2014 Nov 7	⋯	⋯
8394589	9.4	2014 Aug 21	Yes	⋯
8424992	10.1	2014 Jul 13	⋯	⋯
8524425	9.5	2014 Jul 11	⋯	⋯
8561221	9.6	2014 Jul 13	⋯	⋯
8694723	8.7	2014 Jul 13	⋯	⋯
8702606	9.1	2014 Jul 13	⋯	⋯
8751420	…	2014 Jul 13	⋯	⋯
8760414	…	2014 Jul 13	⋯	⋯
9025370	8.7	2014 Jul 13	⋯	⋯
9073950	11.1	2014 Jul 13	⋯	⋯
9098294	9.6	2014 Jul 13	⋯	⋯
9139151	9.0	2014 Jul 13	⋯	⋯
9139163	8.2	2014 Jul 13	Yes	⋯
9206432	9.0	2014 Jul 13	Yes	⋯
9353712	…	2014 Jul 13	⋯	⋯
9410862	10.6	2014 Jul 13	⋯	⋯
9414417	9.5	2014 Jul 13		K00974.01
9574283	10.5	2014 Jul 13	⋯	⋯
9812850	9.4	2014 Jul 13	⋯	⋯
9955598	9.2	2014 Jul 13	⋯	K01925.01
10018963	8.6	2014 Jul 13	⋯	⋯
10068307	8.1	2014 Jul 13	⋯	⋯
10079226	9.9	2014 Jul 13	⋯	⋯
10130853	10.6	2014 Jul 13	⋯	⋯
10147635	10.5	2014 Jul 13	⋯	⋯
10162436	8.5	2014 Jul 12	⋯	⋯
10272858	11.1	2014 Sep 2	⋯	K05782.01
10454113	8.5	2014 Jul 13	⋯	⋯
10516096	9.3	2014 Jul 17	⋯	⋯
10593351	10.6	2014 Jul 13	⋯	⋯
10644253	9.0	2014 Jun 15	⋯	⋯
10709834	9.7	2014 Jun 17	⋯	⋯
10963065	8.7	2014 Sep 3	⋯	K01612.01
10972873	10.5	2014 Jul 13	⋯	⋯
11026764	9.1	2014 Jul 13	Yes	⋯
11081729	9.0	2014 Jul 13	⋯	⋯
11137075	10.7	2014 Jul 13	⋯	⋯
11193681	10.5	2014 Jul 13	⋯	⋯
11244118	9.5	2014 Jul 13	⋯	⋯
11253226	8.4	2014 Jul 13	⋯	⋯
11414712	…	2014 Jul 13	⋯	⋯
11554100	8.4	2014 Jul 13	Yes	⋯
11717120	11.1	2014 Jul 13	⋯	⋯
11771760	9.0	2014 Jul 13	⋯	⋯
11968749	11.2	2014 Jul 13	⋯	⋯
12009504	10.1	2014 Jul 13	⋯	⋯
12069127	9.2	2014 Jul 13	⋯	⋯
12069424	10.5	2014 Jul 13	⋯	⋯
12069449	…	2014 Jul 13	⋯	⋯
12258514	…	2014 Jul 13	⋯	⋯
12307366	11.2	2014 Jul 13	⋯	⋯
12317678	8.6	2014 Jul 13	⋯	⋯
12508433	9.3	2014 Jul 13	⋯	⋯

Note. References for previous detections are denoted using the following codes: (A+) for (Adams et al. 2012; Howell et al. 2012; Wang et al. 2014; Ginski et al. 2016; Kraus et al. 2016), and (CFOP) for high-angular-resolution images available on *Kepler* Community FollowUp Observing Program.

Candidate Survey sample (comprising >90% of the KOI catalog, Law et al. 2014; Baranec et al. 2016; Ziegler et al. 2016) to determine if there is a fundamental difference between them.

The number of candidate companion systems divided by the size of the sample produces the candidate companion fractions. Errors on these fractions are determined using binomial statistics (e.g., Burgasser et al. 2003). While both surveys use Robo-AO and observe KICs, the asteroseismic sample is brighter, has a narrower range of effective temperatures, and, on average, is observed in better conditions.

Overall, for separations out to 2.″5, the asteroseismic sample has a lower companion fraction than the KOI sample and they do not agree within 1σ error ($4.0\%^{+3.0\%}_{-1.2\%}$ and $8.7\%^{+0.5\%}_{-0.5\%}$, respectively).

To determine a more comparable companion fraction for the KOI sample, we combined data from each of the KOI surveys and removed all stars with spectral types inconsistent with the asteroseismic sample. This meant removing all KOIs less than 3900 K and above 7600 K.

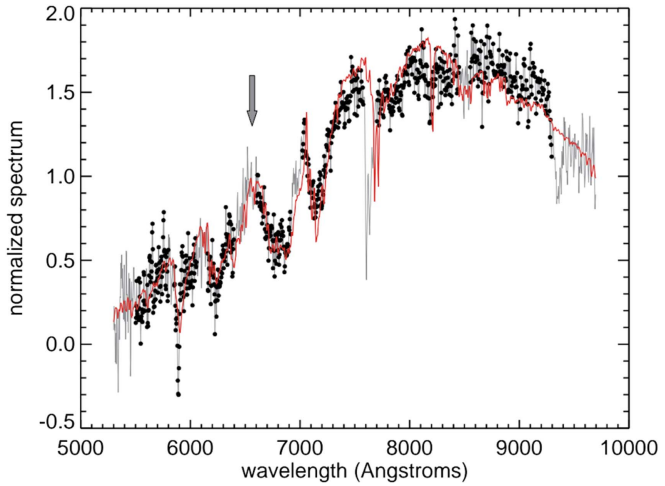

Figure 9. SNIFS red-channel spectrum of the putative M dwarf companion of KIC 5955122. The gray line indicates the complete spectrum, including telluric-affected regions. The black points are the points used for fitting, and the red line is the best-fit PHOENIX model spectrum, with $T_{\rm eff} = 3200$ K, $\log g = 5$, and [Fe/H] $= -0.5$. The arrow indicates the location of any possible Hα emission.

Asteroseismic stars on average appear brighter than KOI stars, so we further restricted the KOI sample by primary star magnitude. Restricting the sample in the i'-band results in stars between 7.1 and 11.3 mag, making it consistent with the asteroseismic sample. When restricting by both temperature and magnitude the companion fraction for the KOI sample rose to $13.8\%^{+9.0\%}_{-5.8\%}$. We did not include stars without an observed i'-band magnitude.

This is unexpected as the asteroseismic sample survey comprises deeper contrast images on average and should therefore produce more candidate companions than the KOI survey. This discrepancy could be due to several factors, e.g., an astrophysical mechanism preventing asteroseismic stars from developing binary companions, small number statistics, or from a biased selection process for the the standard and/or KOI stars, due to small number statistics. We plan to survey the remaining standard stars list ($N \sim 400$) in order to confirm if this discrepancy is real.

7. Conclusion

We used Robo-AO to observe 99 *Kepler* stars that demonstrate stellar oscillations and found eight candidate companion systems that dilute the oscillation amplitudes of their primary light curves. Amplitude dilution values among these stars range from 0.43% to 15.4% and does not explain the excess scatter in the relationship between asteroseismic oscillation amplitudes and the frequency of maximum power (Huber et al. 2011; Corsaro et al. 2013).

Using additional IR photometry, we calculated the photometric distances to the secondary sources of the candidate companion systems. We found that two of the secondary sources are likely foreground objects and at least six of the secondaries are background sources; however, we cannot exclude the possibility that three of these may be physically associated. The measured companion fraction of our *Kepler* asteroseismic sample is $4.0\%^{+3.0\%}_{-1.2\%}$ (for separations out to $2\farcs5$) and is lower than that found for KOIs. A larger sample of asteroseismic stars is needed to determine if this is an astrophysical, bias and/or small sample effect.

We will use Robo-AO (now at the Kitt Peak 2.1 m telescope; Salama et al. 2016) to observe the remainder of the standard stars list, the Gold priority stars, to also determine whether these stars have binary companions or secondary sources within their *Kepler* photometric apertures.

Table 5
Full IR Observations

KIC ID	Obs. Date	Instrument	Total Exposure Time (s)	Companion?
2852862	2016 Apr 16	NIRC2	45	…
3735871	2016 Apr 16	NIRC2	90	…
5184732	2016 Apr 16	NIRC2	45	…
5955122	2016 Jun 17	IRCS	1680	Yes
7747078	2016 Jun 17	IRCS	4.12	Yes
8394589	2016 Jun 17	IRCS	944	Yes
9139163	2016 Jun 17	IRCS	472	Yes
11026764	2016 Jun 17	IRCS	2.45	Yes
11554100	2016 Apr 16	NIRC2	45	Yes
7584900	2016 Sep 13	NIRC2	180	Yes
9206432	2016 Jun 17	IRCS	1	…
	2016 Sep 12	NIRC2	120	Yes

This research is supported by the NASA Exoplanets Research Program, grant #NNX 15AC91G. J.S. acknowledges the UK. S.L.C. C.B. acknowledges support from the Alfred P. Sloan Foundation. We thank Joanna Bulger for helping with the Subaru observations.

The Robo-AO system was developed by collaborating partner institutions, the California Institute of Technology and the Inter-University Centre for Astronomy and Astrophysics, and with the support of the National Science Foundation under grant Nos. AST-0906060, AST-0960343, and AST-1207891, the Mt. Cuba Astronomical Foundation, and by a gift from Samuel Oschin. Some of the data presented herein were obtained at the W.M. Keck Observatory, which is operated as a scientific partnership among the California Institute of Technology, the University of California, and the National Aeronautics and Space Administration. The Observatory was made possible by the generous financial support of the W.M. Keck Foundation. This work is based in part on data collected at Subaru Telescope, which is operated by the National Astronomical Observatory of Japan. SNIFS on the UH 2.2 m telescope is part of the Nearby Supernova Factory project, a scientific collaboration among the Centre de Recherche Astronomique de Lyon, Institut de Physique Nucleaire de Lyon, Laboratoire de Physique Nucleaire et des Hautes Energies, Lawrence Berkeley National Laboratory, Yale University, University of Bonn, Max Planck Institute for Astrophysics, Tsinghua Center for Astrophysics, and the Centre de Physique des Particules de Marseille. The authors recognize and acknowledge the very significant cultural role and reverence that the summit of Maunakea has always had within the indigenous Hawaiian community. We are most fortunate to have the opportunity to conduct observations from this mountain.

Facilities: PO:1.5m (Robo-AO), Keck:II (NIRC2-NGS), Subaru (IRCS), UH:2.2m (SNIFS).

ORCID iDs

Jessica S. Schonhut-Stasik https://orcid.org/0000-0002-1043-8853
Christoph Baranec https://orcid.org/0000-0002-1917-9157
Daniel Huber https://orcid.org/0000-0003-4894-9779
Carl Ziegler https://orcid.org/0000-0002-0619-7639
Dani Atkinson https://orcid.org/0000-0001-8589-1938
Nicholas M. Law https://orcid.org/0000-0001-9380-6457
Reed Riddle https://orcid.org/0000-0002-0387-370X
Janis Hagelberg https://orcid.org/0000-0002-1096-1433
Klaus W. Hodapp https://orcid.org/0000-0003-0786-2140

References

Adams, E. R., Ciardi, D. R., Dupree, A. K., et al. 2012, AJ, 144, 42
Aerts, C., Christensen-Dalsgaard, J., & Kurtz, D. W. 2010, Asteroseismology (Berlin: Springer)
Aldering, G., Adam, G., Antilogus, P., et al. 2002, Proc. SPIE, 4836, 61
Appourchaux, T., Antia, H. M., Benomar, O., et al. 2014, A&A, 566, A20
Atkinson, D., Baranec, C., Ziegler, C., Law, N., & Morton, T. 2017, AJ, 153, 25
Auvergne, M., Bodin, P., Boisnard, L., et al. 2009, A&A, 506, 411
Baranec, C., Riddle, R., Law, N. M., et al. 2013, Journal of Visualized Experiments, 72, e50021
Baranec, C., Riddle, R., Law, N. M., et al. 2014, ApJL, 790, L8
Baranec, C., Ziegler, C., Law, N. M., et al. 2016, AJ, 152, 18
Bedding, T. R., Huber, D., Stello, D., et al. 2010, ApJL, 713, L176
Bedding, T. R., Mosser, B., Huber, D., et al. 2011, Natur, 471, 608
Borucki, W. J., Koch, D., Basri, G., et al. 2010, Sci, 327, 977
Burgasser, A. J., Kirkpatrick, J. D., Reid, I. N., et al. 2003, ApJ, 586, 512
Buton, C., Copin, Y., Aldering, G., et al. 2013, A&A, 549, A8
Campante, T. L., Barclay, T., Swift, J. J., et al. 2015, ApJ, 799, 170
Campante, T. L., Chaplin, W. J., Lund, M. N., et al. 2014, ApJ, 783, 123
Cardelli, J. A., Clayton, G. C., & Mathis, J. S. 1989, ApJ, 345, 245
Cenko, S. B., Fox, D. B., Moon, D. S., et al. 2006, PASP, 118, 1396
Chaplin, W. J., Appourchaux, T., Elsworth, Y., et al. 2010, ApJL, 713, L169
Chaplin, W. J., Basu, S., Huber, D., et al. 2014, ApJS, 210, 1
Christensen-Dalsgaard, J. 2014, Lecture Notes on Stellar Oscillations, Danmarks Grundforskningsfond: Institut for Fysik og Astronomi, Aarhus Universitet Teoretisk Astrofysik Center, http://astro.phys.au.dk/~jcd/oscilnotes/
Corsaro, E., Fröhlich, H.-E., Bonanno, A., et al. 2013, MNRAS, 430, 2313
Davies, G. R., Silva Aguirre, V., Bedding, T. R., et al. 2016, MNRAS, 456, 2183
Deheuvels, S., García, R. A., Chaplin, W. J., et al. 2012, ApJ, 756, 19
Dupuy, T. J., Kratter, K. M., Kraus, A. L., et al. 2016, ApJ, 817, 80
García, R. A., Mathur, S., Pires, S., et al. 2014, A&A, 568, A10
Gilliland, R. L., Jenkins, J. M., Borucki, W. J., et al. 2010, ApJL, 713, L160
Ginski, C., Mugrauer, M., Seeliger, M., et al. 2016, MNRAS, 457, 2173
Hacking, P., Herter, T., Stacey, C., et al. 1997, in ASP Conf. Ser. 124, Diffuse Infrared Radiation and the IRTS, ed. H. Okuda, T. Matsumoto, & T. Rollig (San Francisco, CA: ASP), 432
Handler, G. 2013, in Planets, Stars and Stellar Systems Vol. 4, ed. T. D. Oswalt & M. A. Barstow (Dordrect: Springer), 207
Hekker, S., Gilliland, R. L., Elsworth, Y., et al. 2011, MNRAS, 414 2594
Holwards, J. 1642, Epitome Astronomiae Reformatae, Generalis (I. Albertus)
Houdek, G., Balmforth, N. J., Christensen-Dalsgaard, J., & Gough, D. O. 1999, A&A, 351, 582
Howell, S. B., Rowe, J. F., Bryson, S. T., et al. 2012, ApJ, 746, 123
Huber, D., Bedding, T. R., Stello, D., et al. 2011, ApJ, 743, 143
Husser, T.-O., Wende-von Berg, S., Dreizler, S., et al. 2013, A&A, 553, A6
Kjeldsen, H., & Bedding, T. R. 1995, A&A, 293, 87
Kraus, A. L., & Hillenbrand, L. A. 2007, AJ, 134, 2340
Kraus, A. L., Ireland, M. J., Huber, D., Mann, A. W., & Dupuy, T. J. 2016, AJ, 152, 8
Lafrenière, D., Marois, C., Doyon, R., Nadeau, D., & Artigau, É. 2007, ApJ, 660, 770
Lai, D. 1997, ApJ, 490, 847
Lantz, B., Aldering, G., Antilogus, P., et al. 2004, Proc. SPIE, 5249, 146
Law, N. M., Morton, T., Baranec, C., et al. 2014, ApJ, 791, 35
Mann, A. W., Feiden, G. A., Gaidos, E., Boyajian, T., & von Braun, K. 2015, ApJ, 804, 64
Mann, A. W., Gaidos, E., & Ansdell, M. 2013, ApJ, 779, 188
Mathur, S., Huber, D., Batalha, N. M., et al. 2017, ApJS, 229, 30
Metcalfe, T. S., Creevey, O. L., Doğan, G., et al. 2014, ApJS, 214, 27
Mosser, B., Elsworth, Y., Hekker, S., et al. 2012, A&A, 537, A30
Polfliet, R., & Smeyers, P. 1990, A&A, 237, 110
Riddle, R. L., Hogstrom, K., Papadopoulos, A., Baranec, C., & Law, N. M. 2014, Proc. SPIE, 9152, 91521E
Riddle, R. L., Tokovinin, A., Mason, B. D., et al. 2015, ApJ, 799, 4
Salama, M., Baranec, C., Jensen-Clem, R., et al. 2016, Proc. SPIE, 9909, 99091A
Schwarzenberg-Czerny, A., Weiss, W., Moffat, A., et al. 2010, in COSPAR Meeting 38, paper E23-0017-10
Springer, O. M., & Shaviv, N. J. 2013, MNRAS, 434, 1869
Stello, D., Huber, D., Bedding, T. R., et al. 2013, ApJL, 765, L41
Stello, D., Huber, D., Kallinger, T., et al. 2011, ApJL, 737, L10
Verner, G. A., Chaplin, W. J., Basu, S., et al. 2011, ApJL, 738, L28
Walker, G., Matthews, J., Kuschnig, R., et al. 2003, PASP, 115, 1023
Wang, J., Fischer, D. A., Xie, J.-W., & Ciardi, D. R. 2014, ApJ, 791, 111
Ziegler, C., Law, N. M., Baranec, C., et al. 2016, Proc. SPIE, 9909, 99095U